Journal of
Materials Chemistry A

Materials for energy and sustainability

Accepted Manuscript

This article can be cited before page numbers have been issued, to do this please use: J. Wang, H. Cao, A. L. Hector, N. Zhelev and A. E. Russell, *J. Mater. Chem. A*, 2026, DOI: 10.1039/D6TA00666C.

ROYAL SOCIETY OF CHEMISTRY

rsc.li/materials-a

View Article Online
DOI: 10.1039/D6TA00666C

A lithiophilic TiN-carbon scaffold for lithium-metal anodes, with SEI ionic conductivity boosted by Li_3N formation

Junren Wang, Huaxin Cao, Nikolay Zhelev, Andrea E. Russell, Andrew L. Hector*

School of Chemistry and Chemical Engineering, University of Southampton, SO17 1BJ, UK.
A.L.Hector@soton.ac.uk

Abstract

Self-supporting TiN-modified carbon fibre electrodes (TiN@C) were prepared by a simple nitriding process and tested as lithiophilic, 3D, conductive skeletons. The TiN@C hosts have homogenously distributed lithiophilic nucleation sites and develop a Li_3N-rich secondary electrolyte interphase layer with high ionic conductivity. Their improved kinetic performance relative to carbon frameworks, including charge and mass transfer processes, are explored through various electrochemical tests, *ex situ* characterisation of the electrodes and theoretical calculations. The assembled TiN@C electrodes achieve a dendrite-free morphology even at a relatively high capacity of 20 mA h cm^{-2}. The high electronic conductivity of TiN@C and ionic conductivity of the Li_3N formed *in situ* improve charge and mass transfer. The electrodes achieve a Coulombic efficiency over 99.3% and outstanding lifetime over 200 cycles with a low electroplating overpotential of -15 mV *vs* Li/Li^+. Lithiated Li@TiN@C based symmetric cells and full cells assembled with $LiFePO_4$ both exhibit better cycling stability and rate performance compared with Li@C cells made similarly.

Introduction

Traditional lithium-ion batteries (LIBs) with graphite anodes are likely to provide only moderate further increases in energy density.[1, 2] Lithium metal anodes have extremely high theoretical capacity of 3860 mA h g^{-1} and the lowest potential of -3.04 V vs. standard hydrogen electrode (SHE) among all the potential anodes. Hence, lithium metal batteries (LMBs) are a strong contender to be the next-generation battery of choice.[3, 4] However, current lithium metal anodes (LMAs) present two main challenges.[5-7] On the one hand, lithium metal is strongly inclined to grow as lithium dendrites during the deposition process, resulting in the generation of "dead Li", internal short circuits, and even fires. On the other hand, large volume fluctuations during deposition and stripping processes can cause ruptures in the solid electrolyte interphase (SEI), leading to unstable interfacial structures and deterioration of the electrochemical properties. These challenges have impeded the practical application of the lithium metal anode.

Approaches to improving lithium-metal anode performance include moderating the composition of the SEI film using electrolyte additives, fabricating solid electrolytes with a high Young's

View Article Online
DOI: 10.1039/D6TA00666C

modulus, and inducing homogeneous Li nucleation based on lithiophilic sites at the electrode surface.[8-13] The use of three-dimensional (3D) metal or carbon current collectors can inhibit the growth of lithium dendrites as the increased surface area reduces local current densities, while reducing SEI rupture and structure collapse related to lithium volume changes.[9] However, pure metal or carbon substrates exhibit poor affinity for lithium and often require addition of lithiophilic sites through surface modification to guide lithium nucleation. A variety of lithiophilic modifications have been designed including metal seeds, elemental doping, and addition of oxides, carbides, and nitrides.[14-18] Metal nitrides have high conductivity, may be lithiophilic and hence reduce the overpotential for Li nucleation, and also may facilitate Li^+ ionic conductivity at the surface by Li_3N formation through conversion reactions with Li.[16, 19] Zhu *et al*. prepared a Ni_xN layer on Ni foam by a plasma nitriding process at 450 °C and observed enhanced lithiophilicity.[20] Hou *et al*. produced a CrN-coated 3D stainless steel host by a plasma process and observed formation of Li_3N during conversion reactions,[16] and Luo *et al* similarly found conversion to Li_3N with Mo_2N nanoparticles on carbon fibres.[21]

Notably, TiN has higher electrical conductivity (3.70×10^6 S m^{-1}) than Mo_2N (2.97×10^4 S m^{-1}).[22] Rapid charge transfer through the electrode combined with accelerated Li^+ ion transfer facilitated by Li_3N formation at the electrode interface facilitate both charge transfer and mass transfer processes. Two previous studies examined TiN-carbon composites: for lithium-metal anodes Lin *et al* produced TiN nanoparticle-decorated carbon nanofibers by electrospinning[23] and Fang *et al* made TiN nanorod arrays on carbon textiles via hydrothermal processing followed by a calcination with ammonia.[24] Both exhibited enhanced electrochemical performances achieved by a synergistic effect of lithiophilic TiN and higher surface area. However, there was no detection of Li_3N on either of these TiN-carbon anodes after cycling.

Herein, we report self-supporting TiN nanoparticle-loaded carbon fibre electrodes (denoted as TiN@C), produced via a simple carbothermal nitridation process, as a host for Li deposition, and investigate the nucleation behaviour of Li using both theoretical calculations and experimental characterisation. Electrochemical tests and a series of tests of SEI composition (*ex situ* XRD, *ex situ* XPS and SEM-Raman) are employed to demonstrate the *in situ* formation of a Li_3N-rich SEI film when TiN nanoparticles were present in the anode material. TiN and the formed Li_3N show high Li affinity resulting in a homogeneous Li deposition. The detailed kinetic performance including charge and mass transfer processes are explored through cyclic voltammetry (CV), linear sweep voltammetry (LSV), electrochemical impedance spectroscopy (EIS) and galvanostatic intermittent titration technique (GITT). The 3D structure provides space for Li deposition to avoid large volume changes, and the large specific surface area reduces the local electrode current density. Consequently, the Li nucleation behaviour is effectively regulated, and the achieved dendrite-free Li deposition capacity can be as high as 20 mA h cm^{-2}. The electrochemical performance of TiN@C anodes in half cells is therefore significantly improved,

View Article Online
DOI: 10.1039/D6TA00666C

with stable cycling observed over 200 cycles at 2 mA cm^{-2} and a high CE of 99.3%. This TiN@C anode after loading Li by electrodeposition can perform over 1000 h cycling in symmetrical cells at 0.5 mA cm^{-2} without a large overpotential. The full cells coupled with $LiFePO_4$ also deliver excellent cycling stability and rate performance, suggesting they have great promise for practical applications.

Results and Discussion

Fabrication and characterisation

The 3D carbon skeleton (C) was obtained by carbonising commercial cellulose filter papers under nitrogen at 1400 ˚C. The 3D TiN@C hosts were synthesised by first reacting hydroxide groups on the cellulose with $TiCl_4$ in hexane, so that TiN nanocrystals form by a carbothermal process during the high temperature firing of the carbon (Figure 1a).[15, 25] TiN loading can be adjusted by varying the amount of $TiCl_4$ used in the synthesis process (Table 1). The C and all the TiN@C hosts can be directly used as self-supported, binder-free electrodes after simply punching to size, and are mechanically robust (Figure S1).

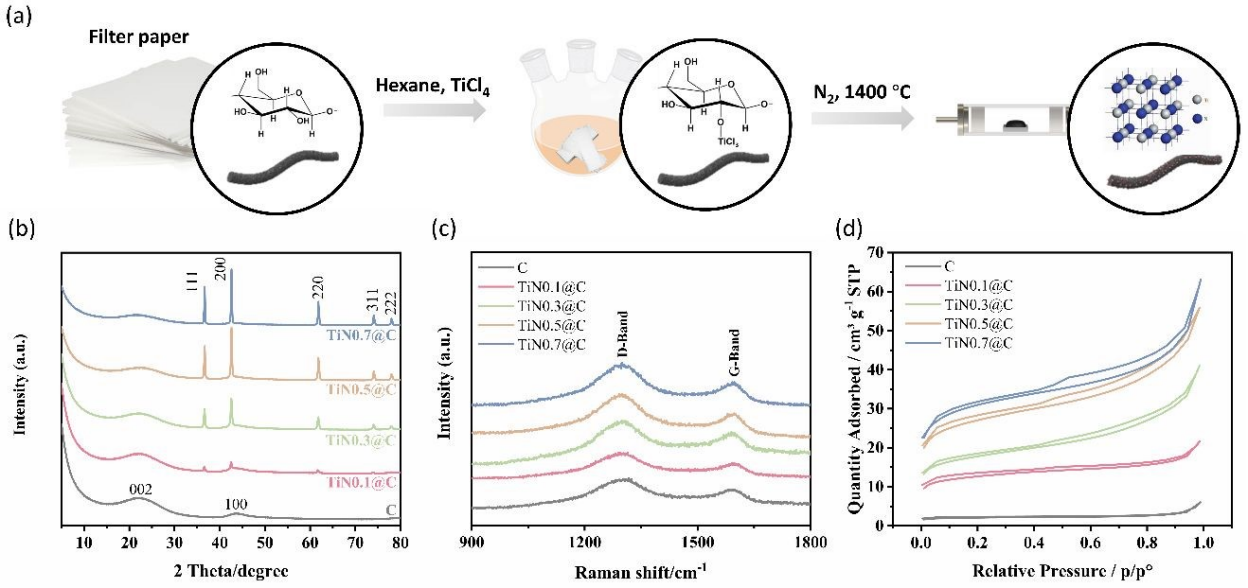

Fig. 1. (**a**) Schematic illustration of the synthesis process of TiN@C; (**b**) XRD patterns of carbon (Miller indices from ICSD 18838 2H graphite) and TiN (ICSD 26947)-carbon composites (**c**) Raman patterns and (**d**) N_2 adsorption and desorption isotherms of carbon and TiN@C with different TiN loadings.

X-ray diffraction (XRD) patterns of the C host and the TiN@C composites are shown in Figure 1b. The broad peaks around 23° correspond to the 002 peak of the graphitic domains of the carbon fibres. This peak can be used to calculate the interlayer d-spacing of carbon (Table 1), which was found to increase with titanium loading. A wider interlayer separation has been linked to more facile lithium-ion insertion, which could be expected to improve lithium wetting of the carbon

View Article Online
DOI: 10.1039/D6TA00666C

surfaces and hence provide easier lithium nucleation kinetics for a subsequent Li plating/stripping process. The second broad feature of carbon is also observed around 44°, corresponding to the 100 peak of the graphitic domains. For all the composites, there are another five obvious peaks, with cubic lattice parameters (~4.24 Å) that correspond to TiN (in our previous study[25] we noted that TiC and TiO have parameters in a distinctly different range). As the titanium loading increased, the TiN peaks increased in intensity and became narrower, implying that the crystallite sizes become larger. Raman spectroscopy is particularly useful to investigate the carbon component of the composites, while the XRD is dominated by titanium nitride. In Figure 1c, the Raman profiles show two broad peaks around 1290 and 1580 cm^{-1}, which can be attributed to the disordered (D-band) and ordered graphitic (G-band) parts of the carbon structure, respectively. The integrated intensity of the D-band is stronger than that of the G-band, suggesting that the composites retain the highly disordered graphitic structure of hard carbon. The integrated intensity ratio I_D/I_G goes up from 2.07 to 2.37 (Table 1) with increasing titanium loading in TiN@C composites. This suggests that the presence of TiN in the composites increases disorder.

Table 1. Physical parameters of C and TiN@C composites.

Sample name	$TiCl_4$ volume (mL)	TiN lattice parameter a (Å)	TiN crystallite size (Å)	Carbon I_D/I_G	Surface area ($m^2\ g^{-1}$)	Pore volume ($cm^3\ g^{-1}$)
C	0	n/a	n/a	2.07	6	0.002
2.3 wt% TiN0.1@C	0.1	4.24(7)	250(1)	2.10	37	0.013
8.9 wt% TiN0.3@C	0.3	4.24(4)	264(2)	2.17	53	0.034
15.0 wt% TiN0.5@C	0.5	4.24(2)	353(8)	2.23	83	0.060
25.9 wt% TiN0.7@C	0.7	4.24(1)	463(7)	2.37	92	0.040

The TiN loading in each composite was measured by TGA with an oxidising 60% O_2 gaseous environment in which the carbon is burned away, and the TiN is converted to TiO_2 (Table 1 and Figure S2). The calculated contents of TiN in TiN0.1@C, TiN0.3@C, TiN0.5@C and TiN0.7@C are 2.3 wt%, 8.9 wt%, 15.0 wt% and 25.9 wt%, respectively. This is consistent with the hypothesis that as the amount of precursor introduced increases, so does the actual content of TiN.

N_2 adsorption-desorption measurements (Figure 1d and Table 1) show a typical type-IV behaviour, indicating the coexistence of micropores (<2 nm) and mesopores (2–50 nm). The Brunauer–Emmett–Teller (BET) analysis reveals a specific surface area of 37 $m^2\ g^{-1}$ for TiN0.1@C, 53 $m^2\ g^{-1}$ for TiN0.3@C, 83 $m^2\ g^{-1}$ for TiN0.5@C, and 92 $m^2\ g^{-1}$ for TiN0.7@C which are all higher

View Article Online
DOI: 10.1039/D6TA00666C

than that of the bare C electrode (6 $m^2 g^{-1}$). The specific surface area of the composites increases with increasing TiN content since the nanoparticles significantly roughen the surface of the carbon fibres. According to Sand's model, the time τ at which lithium dendrites begin to grow is inversely related to the current density J. Larger surface areas can extend the Sand's time and hence suppress the formation of Li dendrites due to a decrease in the current density at the anode surface. The pore size distribution (Figure S3) confirms the hierarchically porous structure, with the pore size diameters in the range of 1.5–50.4 nm. The trend of Barrett–Joyner–Halenda (BJH) pore volume is firstly increased and then decreased, 0.013 $cm^3 g^{-1}$ for TiN0.1@C, 0.034 $cm^3 g^{-1}$ for TiN0.3@C, 0.060 $cm^3 g^{-1}$ for TiN0.5@C, and 0.040 $cm^3 g^{-1}$ for TiN0.7@C which are all higher than that of the bare C electrode (0.002 $cm^3 g^{-1}$).

SEM was employed to investigate the effects of different levels of TiN surface modification (Figure 2). The carbon skeleton with an overall thickness of 385 µm after calcining (Figure S4a) forms a cross-linked network of fibres, with a typical fibre diameter of ~8 µm (Figure 2f). The cavities between the interconnected carbon fibres appear to provide space for Li deposition and could mitigate the effects of volume changes during lithium plating and stripping (Figure 2a). The thicknesses of the TiN@C composites are slightly larger due to the introduction of a certain mass ratio of TiN (400 µm for TiN0.1@C, 420 µm for TiN0.3@C, 435 µm for TiN0.5@C, and 445 µm for TiN0.7@C, Figure S4b-e). The morphology of TiN@C is clearly different than that of the pristine carbon framework, indicating a successful decoration of the carbon skeleton with TiN nanoparticles (Figure 2b-2j). As the amount of added Ti precursor is increased, the density of the TiN nanoparticle distribution also increases. TiN0.7@C, with the highest TiN concentration studied, shows a serious aggregation of TiN particles (Figure 2j). Even if these particles are electronically connected after synthesis they may lose contact during cycling. However, the distance between TiN nanoparticles is relatively large with the lowest level of Ti precursor, TiN0.1@C (Figure 2b, g), which may suggest an insufficient amount of active material to provide a high density of lithiophilic sites. TiN0.3@C has smaller distances between the TiN particles (Figure 2c, h), and TiN0.5@C demonstrates a uniform and dense distribution of TiN particles without significant aggregation (Figure 2d, i), with a size range of 113–191 nm (Figure 2l). The homogeneous EDS elemental mapping images of C, N and Ti further support the uniform distribution of highly ordered TiN on the interconnected C skeleton (Figure 2k-o).

View Article Online
DOI: 10.1039/D6TA00666C

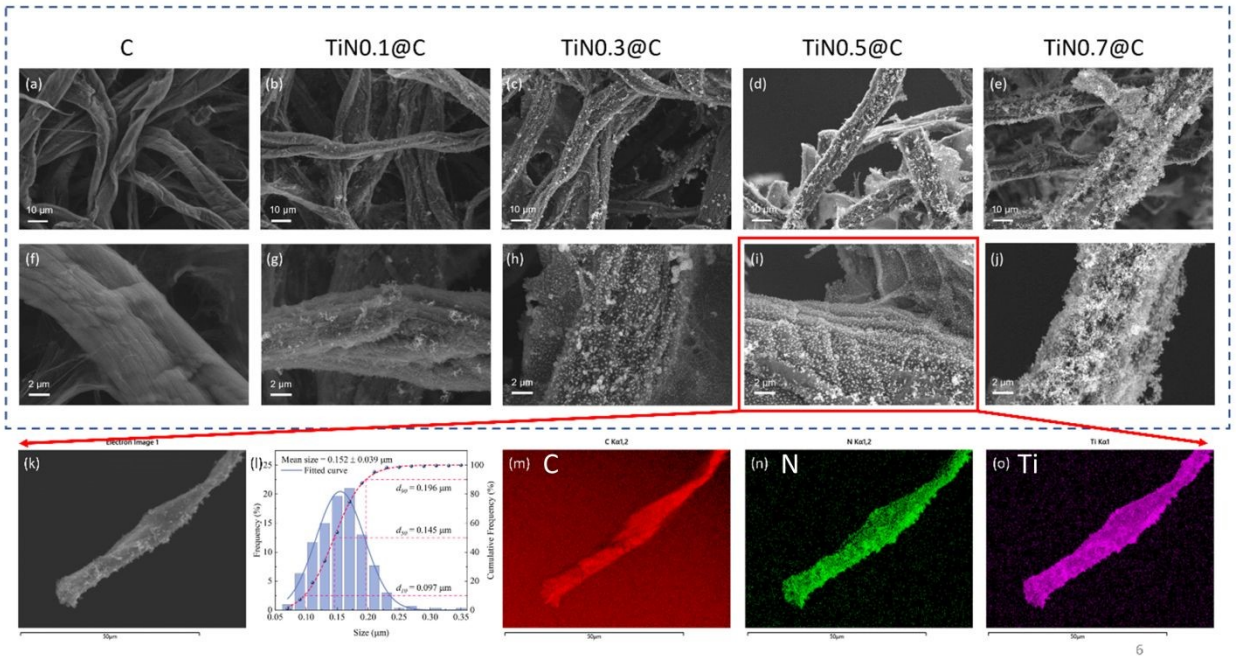

Fig. 2. SEM morphology of (**a, f**) C; (**b, g**) TiN0.1@C; (**c, h**) TiN0.3@C; (**d, i**) TiN0.5@C and (**e, j**) TiN0.7@C; (**k**) Electron image of selected area of TiN0.5@C; (**l**) Particle size distribution of TiN0.5@C; Elemental mapping images for (**m**) C, (**n**) N, and (**o**) Ti of the TiN0.5@C area shown in Figure 2k.

Reversibility of Li plating and stripping

To examine Li plating and stripping at the surfaces of the different electrode types, Li half cells with C and TiN0.5@C working electrodes were fabricated, using a popular ether-based electrolyte (1 M LiTFSI in 1:1, v:v DME and DOL with 1 wt % $LiNO_3$ additive). All half cells underwent an activation process, by cycling between 0-1 V at a small current density (50 µA) for 5 cycles to stabilise the SEI film. After that, a quantity of Li was plated on the working electrodes under a constant current density for a certain length of time, and then the electrodes were stripped at the same current density with a cut-off voltage of 1.0 V.

The intercalation capacities (>0 V vs. Li^+/Li) of C and TiN0.5@C were measured as ~1.1 and ~1.5 mA h cm^{-2}, respectively (Figure S5a). To ensure some plating, the half cells were first tested by loading with lithium to a capacity of 2 mA h cm^{-2} at a current density of 2 mA cm^{-2}. Both C and TiN0.5@C exhibit negligible nucleation overpotential at this relatively low current density and Li areal capacity. The TiN0.5@C//Li half-cell exhibited long-term cycling (lithium deposition and stripping) stability, but the Coulombic efficiency (CE) of the bare C electrode was only maintained for an initial ~100 cycles, and then suddenly decreased (Figure S5b). Hence the TiN appears to have served a positive role in the operation of these electrodes. A high and stable CE often indicates a consistent and uniform lithium deposition.[26] Overpotentials on different modified electrodes under a capacity of 4 mA h cm^{-2} at a current density of 2 mA cm^{-2} were measured to

View Article Online
DOI: 10.1039/D6TA00666C

further verify the effect of TiN loading (Figure 3a). Most of the TiN@C electrodes (TiN0.1@C, TiN0.3@C and TiN0.5@C) exhibit a lower overpotential (-69 mV, -64 mV and -56 mV), compared to that of the bare C electrode (-80 mV) (Figure 3b, c). However the highest TiN loading studied (TiN0.7@C) resulted in the highest overpotential (-94 mV) and a poor CE (Figure 3c, e). The high level of TiN particle aggregation may cause side reactions or surface particles may be poorly connected to the current collector.[27]

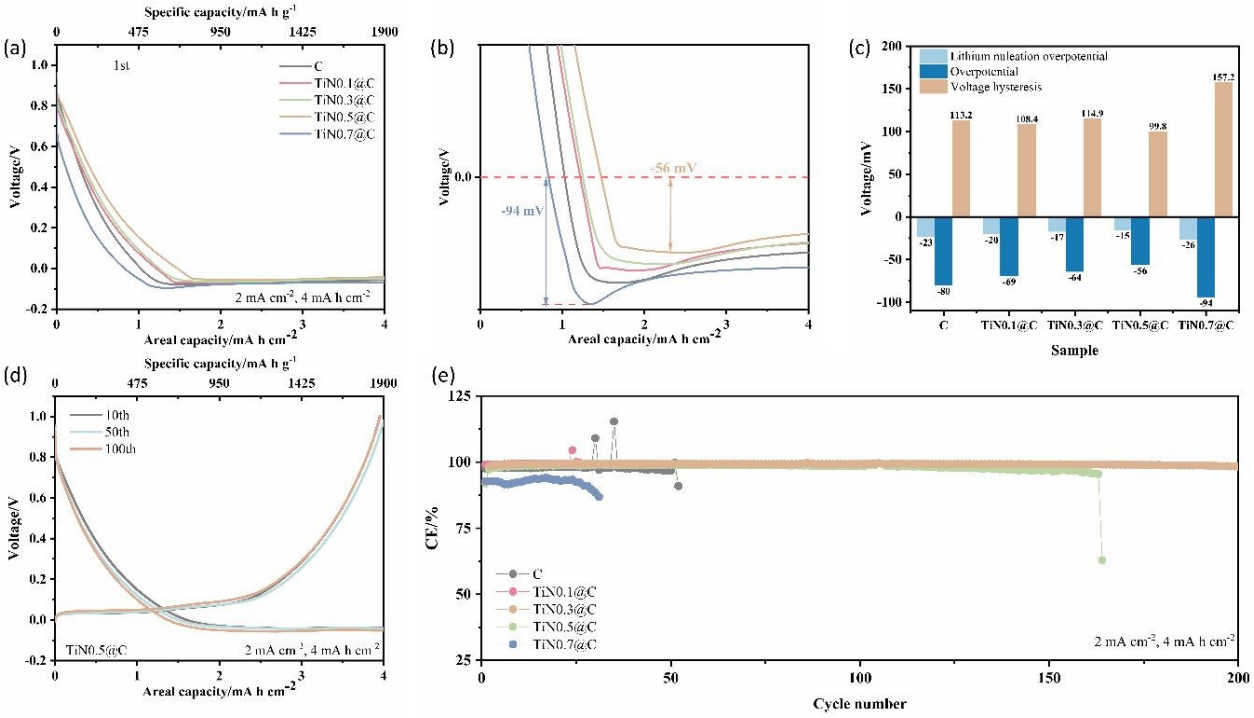

Fig. 3. (**a**) 1st cycle reduction curves of different electrodes under a current density of 2 mA cm^{-2} with a lithium plating capacity of 4 mA h cm^{-2}; (**b**) Enlarged profiles of the selected voltage range shown in (a); (**c**) Summary of the Li nucleation overpotential, overpotential and voltage hysteresis for different electrodes; (**d**) Comparison of voltage profiles of the Li plating/stripping on the TiN0.5@C electrode at different cycles; (**e**) CE of Li plating/stripping on C and different TiN@C electrodes at 2 mA cm^{-2} with a plating capacity of 4 mA h cm^{-2}.

The Li nucleation overpotential is defined as the difference between the highest plating voltage (bottom of the voltage dip) and the stable voltage plateau (Figure S6). This overpotential is the voltage needed to overcome the heterogeneous nucleation barrier caused by the thermodynamic mismatch between lithium and the substrate. As expected, the TiN0.5@C electrode delivers the lowest nucleation overpotential of -15 mV, while the highest overpotential of -23 mV is obtained for the bare C electrode (Figure 3c). Lower TiN loadings (TiN0.1@C, TiN0.3@C) provided smaller reductions in the Li nucleation overpotential due to a more limited number of lithiophilic sites.

View Article Online
DOI: 10.1039/D6TA00666C

After the 50th and 100th charging/discharging process (Figure 3d), there was no obvious change in the overpotentials of TiN0.5@C. Therefore, it can be confirmed that the effect of the TiN on the surface is durable during cycling. The CE (2 mA cm^{-2}, 4 mA h cm^{-2}) for the bare C electrode (~97.7%) was only maintained for the first 50 cycles, and then gradually decreased (Figure 3e). In the case of TiN0.1@C and TiN0.3@C, due to the introduction of lithiophilic TiN active sites, the CE value is better than C. However, the long-term cycling stability is still limited. In contrast, the TiN0.5@C electrode displayed a stable average CE around 99.3% over more than 200 cycles. To further investigate the performance of the TiN0.5@C electrodes in more rigorous conditions, the current was increased to 4 mA cm^{-2}, and the fixed capacity kept as 4 mA h cm^{-2}. The TiN0.5@C electrode still showed excellent cyclability with average CE of 99.1% for 80 cycles at 4 mA cm^{-2} (Figure S7), which was much higher than that of the C electrode.

Voltage hysteresis affects the voltage gap between the Li metal deposition and dissolution profiles and consists of activation, ohmic, and concentration polarisations, where the ohmic and concentration polarisations have a critical effect on the rate capability at higher current rates. The galvanostatic profiles of the C showed a notable voltage hysteresis between the discharge and charge profiles, with the hysteresis increasing notably at the higher areal current rate, suggesting limited rate capability (Figure S8a). In contrast, the voltage hysteresis was significantly reduced with TiN0.5@C (Figure S8b). Even at the higher current rate of 4 mA cm^{-2}, TiN0.5@C maintained a stable voltage hysteresis. Such a lower polarisation is advantageous for lithium metal deposition/dissolution cycling.

Since TiN0.5@C clearly had the best half-cell performance, this composition was used in the subsequent studies, and for simplicity is labelled TiN@C in the remainder of the work.

In situ formation of Li_3N-rich SEI layer

The first reduction galvanostatic voltage-time profiles in the electrode activation process (open circuit potential to 0.0 V vs Na/Na^+ at 50 µA cm^{-2}) of C//Li and TiN@C//Li half-cells are shown in Figure 4a. A larger amount of charge is passed with the TiN@C electrode compared with the C electrode. A cyclic voltammogram (CV) collected with fresh electrodes (0.1 mV s^{-1}; Figure 4b) contained reduction peaks around 0.1 V, expected for Li^+ intercalation into carbon, and 0.8 V corresponding to the reduction of the electrolyte additive $LiNO_3$.[28] There is also a reduction peak at 1.45 V in the TiN@C system that has been attributed to TiN reduction, i.e. a conversion reaction:[29, 30]

$$TiN_{(s)} + 3Li^+_{(soln)} + 3e \rightarrow Li_3N_{(s)} + Ti_{(s)}$$

This process can of course continue through the conditioning cycles carried out between 1.0 and 0.0 V. It can also be observed in the longer voltage plateau at around 1.5 V in TiN@C//Li compared with C//Li in the galvanostatic discharge curves (Figure 4a). The facile reduction of TiN at nanoparticle surfaces may lead to the generation of Li_3N-rich SEI layers in these regions of the

View Article Online
DOI: 10.1039/D6TA00666C

composite. The growing overlap of subsequent CV curves during cycling indicates that the electrodes have good reversible capacity and cycle stability (Figure S9).

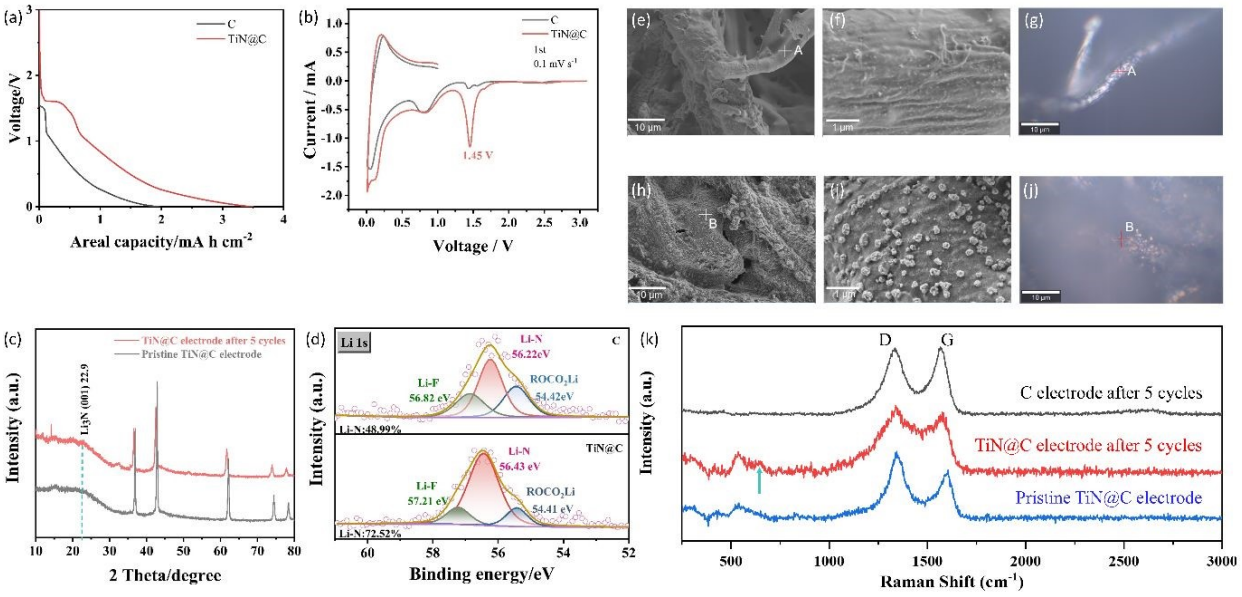

Fig. 4(**a**). The reduction profiles of C/TiN@C electrodes in the 1st activation cycle; (**b**) The CV curves of C and TiN@C electrodes at a scan rate of 0.1 mV s^{-1} from open circuit potential to 0.01 V then 1.0 V; (**c**) *ex situ* XRD patterns of activated TiN@C and pristine TiN@C electrodes; (**d**) *ex situ* XPS patterns of activated C and TiN@C electrodes; SEM morphology of (**e-f**) activated C electrode and (**h-i**) activated TiN@C electrode; Optical morphology of (**g**) activated C electrode and (**j**) activated TiN@C electrode; (**k**) Comparison of Raman patterns of a pristine TiN@C electrode, an activated TiN@C and an activated C electrode (green arrow marks a peak related to Li_3N).

Ex situ XRD and XPS of TiN@C or bare C electrodes after 5 activation cycles were used to probe any changes in TiN after cycling. Samples were rinsed of electrolyte and handled in inert atmosphere before collecting these measurements. As shown in Figure 4c, the main XRD peaks were still attributed to TiN, showing that the bulk of the TiN is unchanged. However, a weak peak at 22.9° shows the presence of Li_3N (001 reflection) showing that some reduction/conversion has occurred.[16] The Li 1s region XPS (Figure 4d top) shows a peak at 56.22 eV corresponding to Li_3N, which comes from reduction of the $LiNO_3$ additive in the electrolyte. The other peaks in the Li 1 s spectrum correspond to ROCOOLi (54.42 eV), and LiF (56.82 eV).[31] In contrast, the content of Li_3N in TiN@C was obviously higher than that observed on the C electrode according to the Li 1s peak fitting (Figure 4d bottom), which suggests the conversion reaction of TiN to Li_3N also plays a significant role in its formation.[16, 32] The morphology of activated C or TiN@C electrodes was examined by SEM (Figure 4e-j) and Raman spectra were collected at specific points (point A in Figure 4g, point B in Figure 4j). The Raman spectrum of the cycled C electrode only contains the

View Article Online
DOI: 10.1039/D6TA00666C

common D and G bands for the carbon. The pristine TiN@C electrode also exhibits Raman peaks in the range 200-580 cm^{-1} corresponding to TiN.[30] The spectrum of the activated TiN@C electrode contains the carbon and TiN features but also an extra Raman signal at 590-640 cm^{-1} (Figure 4k, with an enlarged profile in Figure S10) that is consistent with Li_3N.[33] The strong cycling performance suggests that Li_3N continues to be present at electrode surfaces, which could be due to early formation that persists or to continuous generation from the TiN surfaces.

Li_3N has a high Li^+ conductivity (2×10^{-4} S cm^{-1}) so is expected to promote rapid transport of Li^+ ions. The charge transfer process primarily involves the reduction of Li^+ ions to generate Li atoms. Any acceleration of charge-transfer kinetics during Li deposition (-0.2 V to 0.2 V) due to the increased Li_3N concentration should be visible in the exchange current density and hence via Tafel plots obtained from linear sweep voltammetry (LSV) curves. The TiN@C electrode exhibits a lower overpotential and higher current response, indicating a lower Li plating/stripping barrier and higher electron exchange rate (Figure 5a). Specifically, the exchange current density of the TiN@C anode is determined to be 0.356 mA cm^{-2} from the Tafel curve, which is higher than that of C (0.288 mA cm^{-2}). The higher exchange current density indicates that the TiN@C electrode has better charge transfer capability compared to the C electrode. This should result in a decrease in the electrochemical polarisation at the electrode surface.

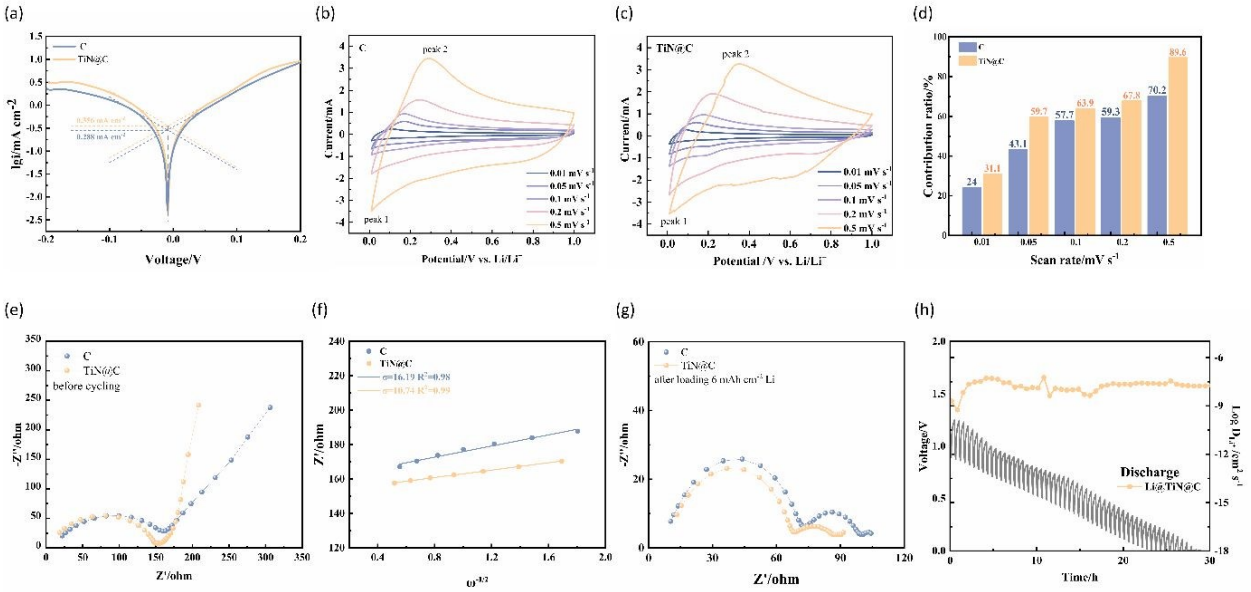

Fig. 5. (**a**) Tafel plots of half cells with bare C and TiN@C electrodes; CV curves of (**b**) C and (**c**) TiN@C electrodes at different scan rates from 0.01-0.5 mV s^{-1}; (**d**) Contribution ratio of capacitive processes at different scan rates of C and TiN@C electrodes; (**e**) EIS of pristine C and TiN@C electrodes before cycling (after 20 h rest); (**f**) The relationship between real parts of the impedance (Z') and the reciprocal square root of the angular frequency (ω) in the low-frequency

View Article Online
DOI: 10.1039/D6TA00666C

region for bare C and TiN@C electrodes; (**g**) EIS of C and TiN@C electrodes after plating 6 mA h cm^{-2} Li; (**h**) GITT profile and the calculated Li^+ diffusion coefficients of Li@TiN@C electrode.

CV measurements at scan rates from 0.01 to 0.5 mV s^{-1} were carried out to assess the capacitive contributions to charge storage with C and TiN@C (Figure 5b, c). All the CV curves exhibit similar shapes. The capacitive effect can be analysed according to a power-law relationship by using the following equation:

$$i = av^b \qquad \text{-Eqn. 1}$$

Where i is the peak current (mA) and v is the scan rate (mV s^{-1}).[34] Both a and b are adjustable constants, and the value of b is determined from the slope of the plot of log(i) versus log(v) (b = 0.5, diffusion-dominated process; b = 1, capacitive process).[35] For peak 1, the b values are 0.73 for C and 0.80 for TiN@C, and for peak 2, the b values are 0.72 for C and 0.83 for TiN@C (Figure S11), suggesting that a mixed process existed in both electrodes but more of the Li^+ ion storage behaviour of TiN@C is linked to capacitive processes. To be more accurate, a quantitative capacitive contribution can be calculated separately according to the work of Dunn:

$$i = k_1v + k_2v^{1/2} \qquad \text{-Eqn. 2}$$

Where k_1 and k_2 are the function of potential, and k_1v and $k_2v^{1/2}$ correspond to capacitive effects and diffusion-controlled insertion, respectively.[36] Both the capacitive contributions in C and TiN@C gradually increase with increasing scan rate as summarised in Figure 5d and capacitive contributions in TiN@C are consistently greater than those in C. The higher capacitance with TiN introduction contributes to fast charge transfer,[37] and can be linked to both the higher surface area and the faster charge transfer process.

Electrochemical impedance spectroscopy (EIS) data can be used to probe charge-transfer and mass-transfer features. EIS results of the pristine electrodes without any cycles showed a common characteristic, a depressed semicircle in the high-medium frequency region (charge transfer resistance, R_{ct}) followed by a sloping Warburg line (Li^+ ions diffusion resistance, W) in the low frequency region (Figure 5e, equivalent circuit diagram as shown in Figure S12). R_{ct} is used to assess the electrode kinetics, where a lower R_{ct} indicates faster kinetics of the redox processes occurring on the electrode material surface. As expected, TiN@C before cycling has a lower R_{ct} (149 Ω) than that of C (159 Ω) (Table S1). The smaller slope of the linear region of TiN@C suggests a lower Li^+ ion diffusion impedance. To further demonstrate the Li^+ diffusion properties, the corresponding linear fit between the real Z' impedance and $\omega^{-1/2}$ at low frequencies is given in Figure 5f, and which also aligns with its lower δ value (10.74) than that of C (16.19). The TiN@C electrode exhibits superior ionic diffusion efficiency, facilitating the rapid diffusion of Li^+ ions from the electrode surface to the inside, owning to the high lithiophilic Li_3N conversion from TiN during the battery activation.

View Article Online
DOI: 10.1039/D6TA00666C

After plating 6 mA h cm^{-2} Li, the EIS (Figure 5g, equivalent circuit diagram as shown in Figure S13) consisted of two semicircles at high frequency, where the first additional semicircle observed could be attributed to SEI resistance (R_{SEI}). The TiN@C electrode after plating 6 mA h cm^{-2} Li with a lower R_{SEI} displays a much smaller semicircle than that of C, indicating good preservation of the SEI layer and high Li^+ conductivity. After the 1st plating/stripping cycle, TiN@C still has a significantly lower interface R_{SEI} and R_{ct} than that of C electrodes (Figure S14).

To further understand the Li^+ diffusion coefficient of the Li@TiN@C electrode, the galvanostatic intermittent titration technique (GITT) was employed, based on the following equation:

$$D_{Li}=\frac{4}{\pi\tau}\left(\frac{n_m V_m}{S}\right)^2\left(\frac{\Delta E_s}{\Delta E_t}\right)^2 \qquad \text{-Eqn. 3}$$

Where τ (s) is the relaxation time, n_m (mol), and V_m (cm^3 mol^{-1}) are the molar mass and volume, S (cm^2) is the electrode surface area, ΔE_s (V) is the voltage variation during current pulse, and ΔE_t (V) is the voltage change during the discharge/charge processes.[38, 39] The Li@TiN@C electrode (Figure 5h) exhibits a higher diffusion coefficient of 10^{-9}–10^{-7} cm^2 s^{-1} than that of Li@C (Figure S15), which is ascribed to the Li^+ ionic conductivity of Li_3N.

Interaction between Li and TiN via simulation

It is meaningful to estimate the lithophilic properties of TiN and *in situ*-formed Li_3N to fully understand the function of the nitriding modification layer. Density functional theory (DFT) calculations are described in the Supporting Information. The binding energies and charge density differences of Li^+ ions on different material surfaces were calculated. It can be observed that the binding energy of lithium ions on bare C is significantly lower than that on the surfaces of Li_3N and TiN (Figure 6). The TiN (200) surface exhibits stronger binding with a Li atom (-2.83 eV) than that of C (-0.65 eV), demonstrating the preferred adsorption of Li atoms on TiN rather than C surface during Li deposition. This is what is referred to as “lithiophilicity”. In addition, the *in situ* formed Li_3N (001) also exhibits a higher Li affinity (-2.17 eV) than the carbon. The electron density difference indicates that this is because the N atoms in Li_3N and TiN can act as Lewis bases to adsorb positively charged Li^+ ions (Figure 6). The electrons of the surface-adsorbed Li^+ ions prefer to transfer to the N atoms in Li_3N or TiN, resulting in higher lithium affinity.

View Article Online
DOI: 10.1039/D6TA00666C

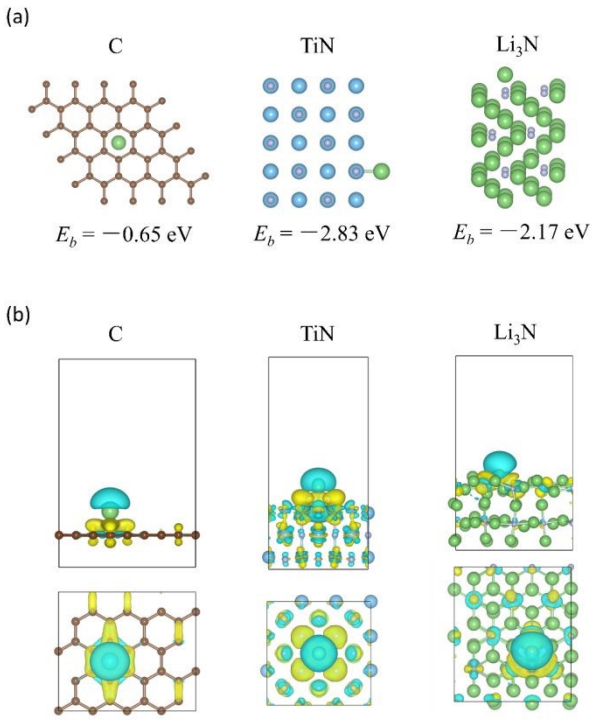

Fig. 6. (**a**) Optimised geometries for calculating the binding energy of a Li atom adsorbed on bare C, TiN and Li_3N; (**b**) the corresponding charge density difference (brown, green, blue, and grey spheres represent C atoms, Li atoms, Ti atoms and N atoms, respectively).

Li deposition behaviours

Ex situ SEM was used to reveal the morphologies of Li deposition. Half cells were assembled with bare C or TiN@C as working electrodes and Li foil as counter electrodes. After plating different area capacities of Li on working electrodes at a current density of 0.5 mA cm^{-2}, the cells were disassembled in the glove box and washed with 1,2-dimethoxyethane (DME) to remove the electrolyte and SEI.

Deposition of 2 mA h cm^{-2} Li results in the formation of a smooth surface (Figure S16b), while on the C electrode Li nucleates randomly on the skeleton resulting in irregular Li deposition (Figure S16a). The smooth surface suggests that Li initially nucleates on the lithophilic TiN nanoparticles and then goes on to fill the gaps between them. EDS analysis was used to confirm TiN was still present in the TiN@C system (Figure S16c). After loading 4 mA h cm^{-2} Li, as shown in the side view (Figure 7a, e), the distribution of Li is across the internal surfaces of the C or TiN@C electrodes, rather than accumulating on the top surface. However, the carbon skeleton surface exhibits limited lithiophilicity, resulting in a significant Li aggregation at bottom of the electrode, close to the current collector (Figure 7d1, d2). This may also related to a lower electronic conductivity of the carbon electrode. Additionally, some local areas of the C skeleton have no Li coverage. The presence of Li aggregation can also be observed in the top and middle layers of

View Article Online
DOI: 10.1039/D6TA00666C

the C electrode (Figure 7b1-c2). On the contrary, the TiN@C skeleton (Figure 7h1, h2) was covered with dense Li. Lithium is effectively accommodated throughout the electrode and forms a uniform and smooth connection to the skeleton. No irregular lithium deposits were found in the top and middle layers (Figure 7f1, g1), and local magnification of the skeleton shows a uniform lithium metal plating (Figure 7f2, g2). After loading 8 mA h cm^{-2} Li, uncontrollable Li clusters begin to appear on the C electrode (Figure S17a), while the TiN@C maintains a regularly smooth surface (Figure S17b). As Li deposition increases further, more Li subsequently deposited within the 3D scaffold. After loading 20 mA h cm^{-2} Li, the 3D skeleton is completely covered with lithium (Figure S18), indicating that the capacity limit has been reached.

Windowless EDS (Figure S19) was employed to show that all of the coverage of the electrodes is metallic lithium. This is possible as EDS is a core hole relaxation technique, and for lithium only the metal has an electron that can relax (Li^+ has a $1s^2$ configuration). SEM was also conducted to observe the morphology of different electrodes after cycling. After 100 cycles, dead lithium remains on the carbon skeleton but not on the TiN@C skeleton (Figure S20), indicating the high reversibility of the TiN@C electrode, in line with the CE results.

View Article Online
DOI: 10.1039/D6TA00666C

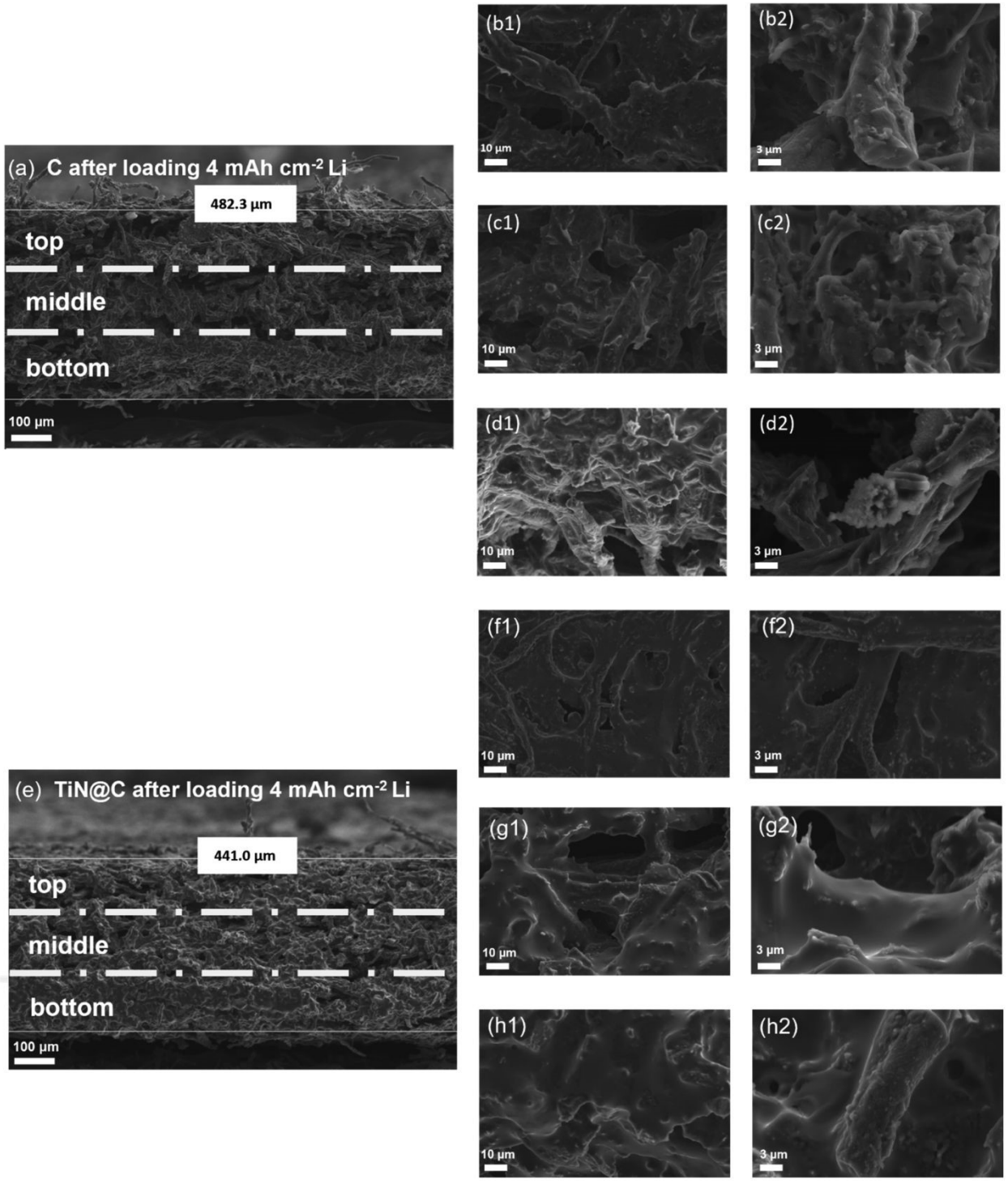

Fig. 7. Different Li deposition behaviours on (top) C and (bottom) TiN@C; Side-view SEM morphology of (**a**) C, (**e**) TiN@C electrodes after plating 4 mA h cm^{-2} Li; Top part of (**b1, b2**) C, (**f1, f2**) TiN@C electrodes; Middle part of (**c1, c2**) C, (g1, g2) TiN@C electrodes; Bottom part of (**d1, d2**) C, (**h1, h2**) TiN@C electrodes.

View Article Online
DOI: 10.1039/D6TA00666C

Electrochemical Performance of Li@TiN@C

Smooth deposition onto TiN@C has been demonstrated, but in a battery the electrode would be subject to repeat plating and stripping cycles. Symmetric cells were employed to evaluate the cycling stability of Li deposits, removing any effect from the counter electrode from consideration. 3D electrodes were preloaded with 6 mA h cm^{-2} Li and used as 3D lithium metal anodes (denoted as Li@TiN@C, with lithium foil (Li) and Li@C as comparisons). As can be seen from Figure 8a, under an applied galvanostatic current of 0.5 mA cm^{-2} and fixed Li deposition amount of 0.5 mA h cm^{-2}, the voltage fluctuation was obvious on a Li metal symmetric cell during cycling. An Li@C symmetric cell exhibits a larger overpotential (187 mV), while a Li@TiN@C symmetric cell displayed a lower overpotential of 109 mV (Figure 8d). After 200 and 450 h, there is an obvious and sudden voltage decrease for the Li and Li@C symmetric cell, respectively, which means there is a short circuit in the cell caused by Li dendrites. Variations of voltage shape have a close connection with the stability of lithium metal electrodes affected by dead Li. In the voltage-time profiles of the selected 30-35th cycles (Figure 8b), the Li symmetric cell displays the highest overpotential, which means an undesirable Li^+ transfer process is operating. Due to the higher surface area, the transfer process of Li^+ can be accelerated in the Li@C symmetric cell and hence the overpotential decreases. After the decoration of lithiophilic TiN sites and the formation of an Li_3N-rich SEI layer with higher Li^+ ionic conductivity, the overpotential is further decreased. Meanwhile, compared to the Li@TiN@C symmetric cell, the voltage of the stripping process of the Li@C symmetric cell continues to increase each cycle, while the voltage is steady in the Li@TiN@C system. When the current remains constant, an increase in voltage indicates a corresponding growth in the internal resistance of the cell. This phenomenon is attributed to the elongation of the Li^+ transfer route during the stripping process, which is caused by the formation of uncontrolled dead Li. The voltage trace of the Li@C symmetric cell deteriorates even further in the 100-105th cycles caused by the expanding dead Li layer (Figure 8c). In contrast, in the Li@TiN@C symmetric cell there is a flatter voltage profile, which shows the higher reversibility of the Li behaviours, and this cell maintains a remarkable lifespan over 1000 h (~450 cycles).

View Article Online
DOI: 10.1039/D6TA00666C

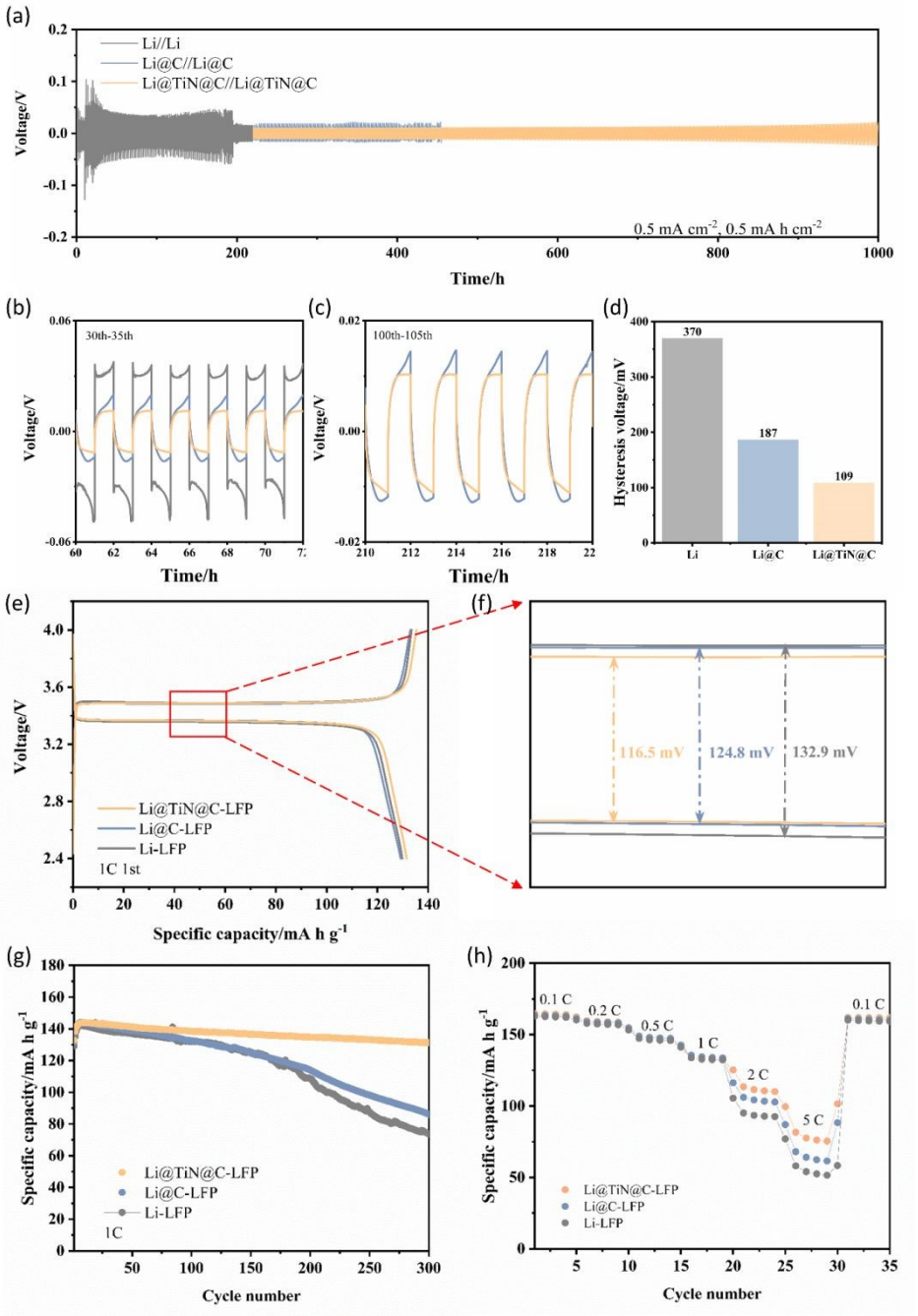

Fig. 8. (**a**) Voltage-time profiles of Li, Li@C, and Li@TiN@C symmetric cells during plating/stripping processes with a 0.5 mA h cm^{-2} capacity and current densities of 0.5 mA cm^{-2}; (**b**) Selected 30-35th voltage-time profiles of different symmetric cells; (**c**) Selected 100-105th voltage-time profiles of different symmetric cells; (**d**) The corresponding hysteresis voltages of different symmetric cells at the 30th cycle; (**e**) The 1st charge–discharge profiles at 1 C of Li@TiN@C-LFP, Li@C-LFP and Li-LFP cells; (**f**) Enlarged profiles exhibiting the polarisation of selected voltage range in figure f; (**g**) Cycling performance of Li@TiN@C-LFP, Li@C-LFP and Li-LFP cells at 1 C; (**h**) Rate performance of Li@TiN@C-LFP, Li@C-LFP and Li-LFP cells.

View Article Online
DOI: 10.1039/D6TA00666C

Full cells paired with a LFP cathode with a mass loading of 1.5 mA h cm^{-2} were initially tested at 1 C in the voltage range of 2.5-4.0 V (Figure 8e). This part of the work used a carbonate electrolyte rather than the ether-based system used for half cells and symmetric cells, to balance stability at both the negative and positive electrode. The ethers would undergo oxidation at the positive electrode. During the first few cycles, the discharge capacities of Li@TiN@C, Li@C and Li cells are very similar, at 131, 129 and 132 mA h g^{-1}, respectively. However, the voltage polarisation between the charge and discharge plateaus of Li@TiN@C-LFP is smaller than that of Li@C-LFP and Li-LFP (Figure 8f), suggesting a sluggish charge-transfer process at the Li/electrolyte interface without TiN modifications. Similar behaviour is observed in the charge/discharge profiles at 2C and 5C (Figure S21). After 300 cycles, the capacity of the Li@C-LFP cell decreases to 87 mA h g^{-1}, offering a low capacity retention of 67.2%. Conversely, high discharge capacities (131 mA h g^{-1}) with enhanced capacity retention of 98.8% were obtained in a Li@TiN@C-LFP full cell after the same cycling process (Figure 8g). Figure 8h shows the notable rate capability differences, especially under high rates. The Li-LFP cell only offers capacities of 95 mA h g^{-1} at 2C and 58 mA h g^{-1} at 5C, whereas the Li@C-LFP cell shows slightly higher capacities of 104 mA h g^{-1} at 2C and 68 mA h g^{-1} at 5C, and the Li@TiN@C cell delivers capacities of 113 mA h g^{-1} at 2C and 81 mA h g^{-1} at 5C. These results indicate that the Li@TiN@C composite electrode effectively reduced the ion transport barrier and the dendrite-free behaviours can greatly improve the long-term cyclability of full cells.

Conclusions

We have fabricated well-distributed TiN nanoparticles on a carbon skeleton with loadings that make them effective as a self-supporting lithiophilic 3D host. The obtained TiN@C hosts have a dual-functional intrinsic advantage of incorporating the homogenously distributed lithophilic nucleation sites and formation of a favourable Li_3N-rich SEI layer with high ionic conductivity. Firstly, there is an abundance of strongly bound TiN nanoparticles on the surface of the carbon skeleton, which enhances the affinity to Li, explained by first-principles calculations, thus ensuring a well-regulated Li nucleation/growth. Meanwhile, a Li_3N-rich SEI layer can be formed *in situ* in the TiN@C system by electrochemically converting TiN into Li_3N, thus improving its Li ionic conductivity. Benefiting from the synergistic effect of both the 3D skeleton and TiN modification, the assembled TiN@C electrodes achieve a dendrite-free morphology even at a high lithium plating capacity of 20 mA h cm^{-2} and effectively accommodate the volume expansion. Furthermore, the high electronic conductivity of TiN@C and ionic conductivity of the Li_3N-rich secondary electrolyte interphase significantly improve the charge and mass transfer process. The resultant electrochemical performance indicators include an extremely high average Coulombic efficiency over 99.3% and outstanding lifetime over 200 cycles with low electroplating overpotential of -15 mV. As a lithium metal anode, after loading 6 mA h cm^{-2} Li in this host, the Li@TiN@C based symmetric cells stably operate over 1000 h at 0.5 mA cm^{-2} for 0.5 mA h cm^{-2}.

View Article Online
DOI: 10.1039/D6TA00666C

Table S2 provides a performance comparison with other nitride-modified materials. Furthermore, the Li@TiN@C anode with limited excess Li paired with LFP cathodes deliver both better rate capability and cycling stability. Our work provides a simple and low-cost nitriding method to fabricate self-supporting nitrides-based carbon electrodes, which shows strong promise for practical applications, and presents a comprehensive analysis of its electrochemical mechanism for the first time.

Materials and Methods

Synthesis process

The TiN@C composites with different ratios of TiN were synthesised by reacting cellulose-based filter paper with $TiCl_4$, then the paper was carbonised in the tube furnace under N_2 atmosphere emulating a process we recently used to make TiN@C powders.[25] In brief, 5 g of filter paper (Thermo Scientific, Western Blotting filter paper WO3259411, cut to strips with 2 cm width) were washed with deionised water three times and dried in an oven at 120 °C overnight. Dried filter paper strips were placed in a flask and flushed in N_2 for 30 mins. Dried hexane (200 mL, Fisher Scientific, distilled from sodium/benzophenone ketyl ether) was transferred into the flask, and then 0.1 mL, 0.3 mL, 0.5 mL or 0.7 mL of $TiCl_4$ (Sigma-Aldrich, 99.9% trace metals basis) was added and stirred for 30 min at room temperature. After refluxing the mixture at 80 °C overnight, the solvent and any remaining precursor were removed *in vacuo*. The dried material was carbonised at 1400 °C for 2 h under N_2 flowing with a temperature ramp rate of 4 °C min^{-1}. A pure carbon sample was synthesised by the direct carbonisation of dried filter paper at 1400 °C for 2 h without any modifying operations.

Characterisation

Powder X-ray diffraction (XRD) patterns were obtained from ground samples employing parallel Cu K_α X-rays in 0.6 mm silica capillaries using a Rigaku Smartlab. XRD data analysis used the Rigaku PDXL2 package. Raman spectra were collected with a Renishaw inVia Raman microscope, coupled with a 785 nm laser, with measurement laser power set to 7.08 mW. Raman peak analysis used WiRE software. Thermogravimetric analysis (TGA) was performed using a Netzsch TG 209 F1 Libra with a ramp rate of 10 °C min^{-1} and a flowing gas combination of Ar (50 mL min^{-1}) and O_2 (20 mL min^{-1}). The surface areas were determined using the Brunauer-Emmet-Teller (BET) technique based on nitrogen adsorption and desorption isotherms measured on a Micromeritics Tristar II surface area analyser. Scanning electron microscopy (SEM) was performed with a ZEISS Sigma 500VP, operated at a 10 kV accelerating voltage. Energy-dispersive X-ray spectroscopy (EDS) analysis used an Oxford Instruments Ultim Extreme 100 mm^2 windowless detector. X-ray photoelectron spectroscopy (XPS) was carried out on a Thermo NEXSA XPS fitted with a monochromated Al K_α X-ray source (1486.7 eV). XPS data analysis was conducted using the Casa

View Article Online
DOI: 10.1039/D6TA00666C

XPS software package. The XPS binding energy scale was calibrated to graphitic carbon at 284.6 eV.

Electrochemical tests

The working electrodes were formed by punching the samples directly into 11 mm diameter disks with average mass of 8.7 mg. Lithium foil disks (CALB Group Co., Ltd, 0.3 mm thickness, 10 mm diameter) were used as the counter and reference electrode. Two sheets of dried Whatman GF/D glass fibre (GE Healthcare Life Sciences) were used as the separator. 1 mol dm^{-3} LiTFSI in dimethoxyethane (DME) / 1,3-dioxolane (DOL) (1:1, v:v) with 1 wt% $LiNO_3$ additive (Duoduo Chem Ltd) was used as the electrolyte for half cells and symmetric cells. The electrolyte for full cells was 1 mol dm^{-3} $LiPF_6$ in ethylene carbonate (EC) / diethyl carbonate (DEC) (1:1, v:v) (Duoduo Chem Ltd). The electrolyte amount for each cell is 120 µL. Two-electrode Swagelok cells were used for all the electrochemical tests, and all the cells were assembled in an argon-filled glovebox (Belle, H_2O < 0.1 ppm, O_2 < 0.1 ppm). A Landhe M340A battery cycler was used to conduct the galvanostatic charge/discharge cycling at 25 °C with a Memmert IPP 55 Plus climatic chamber. Biologic BCS-805 and SP-150 potentiostats were used to conduct electrochemical impedance spectroscopy (EIS), cyclic voltammetry (CV) and linear sweep voltammetry (LSV) with temperature maintained at 25 °C. EIS was obtained in the frequency range from 0.01 Hz to 10 kHz.

The Coulombic efficiency of Li plating and stripping was measured with Li half cells at a current density of 2 or 4 mA cm^{-2} with a fixed charge calculated for an area capacity of 4 mA h cm^{-2}. All half cells were first cycled at 0-1 V at a small current density (50 µA) for 5 cycles to stabilise the SEI film and remove surface contamination. After that, a particular quantity of Li was plated on the working electrodes under a constant current density for a certain length of time, and then the electrodes were stripped at the same current density with a cut-off voltage of 1.0 V. The Coulombic efficiency (CE) was determined by dividing the lithium stripping capacity by the Li plating capacity for each cycle. For symmetric cells and full cells, 6 mA h cm^{-2} Li was first plated on C or TiN@C foam at 0.5 mA cm^{-2} and the cell was disassembled to provide a Li@TiN@C electrode. In symmetric cells, both sides are the Li@TiN@C electrodes and were then charged or discharged for 1 h at different current densities of 0.5 mA cm^{-2} or 1 mA cm^{-2}. For full cells, Li@TiN@C anode, paired with LFP cathode (an areal capacity of 1.50 mA h cm^{-2}) to investigate the practical applications. The $LiFePO_4$ powder (Qinetiq Tatung, C coated) was mixed with super P (carbon black) and polyvinylidene difluoride (PVDF, Solvay) in N-methyl pyrrolidone (NMP, anhydrous, 99.5%, Sigma-Aldrich) with a mass ratio of 8:1:1. Then, the slurry was mixed with a homogeniser (running at speeds of 10,000, 15,000 and 20,000 rpm for 5, 3, and 2 min, respectively) followed by casting onto aluminum foil (15 µm thick, Goodfellow Cambridge Ltd.). The ink was air-dried and then was cut into 11 mm diameter discs and pressed under 5-ton pressure. All the electrodes were dried under vacuum overnight at room temperature before

View Article Online
DOI: 10.1039/D6TA00666C

using. In the full cell tests, 1 C was defined as 170 mA g^{-1} based on the theoretical capacity of $LiFePO_4$.

The Tafel curves of Li||Li symmetrical cells were measured at a scan rate of 1 mV s^{-1} from −0.2 to 0.2 V. The exchange current density was calculated based on the Tafel equation.

$$\eta = a + b \log(j) \qquad \text{-Eqn. 4}$$

where *j* is the current density, η is the overpotential, a and b are constants.

The lithium diffusion coefficient was measured by the galvanostatic intermittent titration technique (GITT). The Li@TiN@C||Cu cell was discharged/charged at a current density of 5 μA for 10 min, followed by an open circuit relaxation for 30 min, and this process was repeatedly conducted. The lithium diffusion coefficient was calculated based on the following equation:

$$D_{Li} = \frac{4}{\pi\tau}\left(\frac{n_m V_m}{S}\right)^2\left(\frac{\Delta E_s}{\Delta E_t}\right)^2 \qquad \text{-Eqn. 5}$$

where τ (s) is the relaxation time, nm (mol), and Vm (cm^3 mol^{-1}) are the molar mass and volume, S (cm^2) is the electrode surface area, ΔE_s (V) is the voltage variation during current pulse, and ΔE_t (V) is the voltage change during the discharge/charge processes.[38, 39]

Computational methodology

All calculations were performed using density functional theory (DFT),[40] as implemented in the VASP (Vienna *ab initio* simulation package)[41] with the Perdew, Burke and Ernzerh (PBE)[42] exchange-correlation potential within the generalised gradient approximation (GGA).[43] The projector augmented wave (PAW) pseudopotential wave was used to describe core electrons.[44] For all optimisation calculations, the convergence criteria for energy and force were set to 10^{-5} eV and 0.01 eV $Å^{-1}$, respectively. The cutoff energy was set to 500 eV, and a gamma-centred 3*3*1 K-point mesh was chosen to describe the Brillouin zone. The (200) surface of TiN was used to represent the interface, as this face has been previously shown to be abundantly exposed in experimental situations.[23] During the structure optimisations, the atoms in the bottom two layers were fixed, while the atoms in the top layers were fully relaxed. A 20 Å vacuum was considered in z-direction of the slab models to prevent the vertical interactions between slabs. The binding energy between the Li atom and the substrates was defined in the following equation:

$$E_{binding} = E_{Li@sub} - E_{sub} - E_{bulk\text{-}Li} \qquad \text{-Eqn. 6}$$

where $E_{Li@sub}$ was the total energy of substrate with an adsorbed Li atom, E_{sub} was the total energy of substrates, and $E_{bulk\text{-}Li}$ was the average energy of a Li atom in bulk state.

Electron density difference calculations were carried out using the CP2K package (version 2024.1), based on PBE functional and a hybrid Gaussian/Plane-Wave scheme (GPW). Molecular orbitals of the valence electrons were expanded into DZVP-MOLOPT-SR-GTH basis sets, while atomic core

View Article Online
DOI: 10.1039/D6TA00666C

electrons were described through Goedecker-Teter-Hutter pseudopotentials. The plane-wave basis set was truncated at the energy cutoff of 500 Ry. The structures were optimised using a tight self-consistent field threshold of 1E-7 arbitrary units. Dispersion correction was applied in all calculations with the DFT-D3 method. Dipole correction was also applied throughout to avoid fictious charge interaction between neighbouring images under the periodic boundary condition. The adsorption energy (E_{ads}) is given by:

$$E_{ads} = E_{total} - (E_A + E_B) \qquad \text{-Eqn. 7}$$

Where E_{total}, E_A, E_B correspond to the energy total systems, slab, and Li atom.

Conflicts of interest

The authors declare no conflict of interest.

Data availability

All data supporting this article will be made available via Southampton's Pure portal (DOI to be added at proof stage).

Acknowledgements

JW thanks the China Scholarship Council for funding. The authors also thank EPSRC for funding equipment used in this work under EP/K00509X/1, EP/K009877/1 and EP/V007629/1.

References

1. L. Zhao, B. Ding, X. Y. Qin, Z. Wang, W. Lv, Y. B. He, Q. H. Yang and F. Kang, *Adv. Mater.*, 2022, **34**, 2106704.
2. J. Liang, F. Li and H. M. Cheng, *Energy Storage Mater.*, 2016, **4**, A1-A2.
3. X. Shen, H. Liu, X. B. Cheng, C. Yan and J. Q. Huang, *Energy Storage Mater.*, 2018, **12**, 161-175.
4. G. Yasin, M. Arif, T. Mehtab, X. Lu, D. Yu, N. Muhammad, M. T. Nazir and H. Song, *Energy Storage Mater.*, 2020, **25**, 644-678.
5. X. Zhang, Y. Yang and Z. Zhou, *Chem. Soc. Rev.*, 2020, **49**, 3040-3071.
6. Y. Guo, H. Li and T. Zhai, *Adv. Mater.*, 2017, **29**, 1700007.
7. Q. Wang, B. Liu, Y. Shen, J. Wu, Z. Zhao, C. Zhong and W. Hu, *Adv. Sci.*, 2021, **8**, 2101111.
8. Y. Li, Y. Li, L. Zhang, H. Tao, Q. Li, J. Zhang and X. Yang, *J. Energy Chem.*, 2023, **77**, 123-136.
9. S. Park, H. J. Jin and Y. S. Yun, *Adv. Mater.*, 2020, **32**, 2002193.
10. G. Lu, J. Nai, D. Luan, X. Tao and X. W. Lou, *Sci. Adv.*, 2023, **9**, eadf1550.
11. Q. Wang, H. Wang, J. Wu, M. Zhou, W. Liu and H. Zhou, *Nano Energy*, 2021, **80**, 105516.
12. Y. Han, B. Liu, Z. Xiao, W. Zhang, X. Wang, G. Pan, Y. Xia, X. Xia and J. Tu, *InfoMat*, 2021, **3**, 155-174.
13. P. Zhai, L. Liu, X. Gu, T. Wang and Y. Gong, *Adv. Energy Mater.*, 2020, **10**, 2001257.
14. B. Liu, Y. Zhang, G. Pan, C. Ai, S. Deng, S. Liu, Q. Liu, X. Wang, X. Xia and J. Tu, *J. Mater. Chem. A*, 2019, **7**, 21794-21801.
15. J. Wang, H. Zhong, B. Liu, M. Zhang, A. L. Hector and A. E. Russell, *J. Mater. Chem. A*, 2023, **11**, 15444-15455.
16. W. Hou, Y. Li, S. Li, Z. Liu, P. R. Galligan, M. Xu, J.-K. Kim, B. Yuan, R. Hu and Z. Luo, *Chem. Eng. J.*, 2022, **441**, 136067.

View Article Online
DOI: 10.1039/D6TA00666C

17. Z. Huang, G. Zhou, W. Lv, Y. Deng, Y. Zhang, C. Zhang, F. Kang and Q.-H. Yang, *Nano Energy*, 2019, **61**, 47-53.
18. P. Zhai, T. Wang, W. Yang, S. Cui, P. Zhang, A. Nie, Q. Zhang and Y. Gong, *Adv. Energy Mater.*, 2019, **9**, 1804019.
19. Y. Han, Z. Sang, D. Liu, T. Zhang, J. Feng, W. Si, S. X. Dou, J. Liang and F. Hou, *Chem. Eng. J.*, 2021, **420**, 129787.
20. J. Zhu, J. Chen, Y. Luo, S. Sun, L. Qin, H. Xu, P. Zhang, W. Zhang, W. Tian and Z. Sun, *Energy Storage Mater.*, 2019, **23**, 539-546.
21. L. Luo, J. Li, H. Yaghoobnejad Asl and A. Manthiram, *Adv. Mater.*, 2019, **31**, 1904537.
22. M. Idrees, A. Mukhtar, S. M. Abbas, Q. Zhang and X. Li, *Mater. Today Commun.*, 2021, **27**, 102363.
23. K. Lin, X. Qin, M. Liu, X. Xu, G. Liang, J. Wu, F. Kang, G. Chen and B. Li, *Adv. Funct. Mater.*, 2019, **29**, 1903229.
24. S. Fang, L. Shen, S. Li, H. Dou and X. Zhang, *J. Mater. Chem. A*, 2020, **8**, 3293-3299.
25. H. Cheng, N. Garcia-Araez, A. L. Hector and S. Soulé, *Inorg. Chem.*, 2019, **58**, 5776-5786.
26. W. Liu, D. Lin, A. Pei and Y. Cui, *J. Am. Chem. Soc.*, 2016, **138**, 15443-15450.
27. C. Wei, B. Xi, P. Wang, Y. Liang, Z. Wang, K. Tian, J. Feng and S. Xiong, *Adv. Mater.*, 2023, **35**, 2303780.
28. S. J. Zhang, Z. W. Yin, Z. Y. Wu, D. Luo, Y. Y. Hu, J. H. You, B. Zhang, K. X. Li, J. W. Yan and X. R. Yang, *Energy Storage Mater.*, 2021, **40**, 337-346.
29. Y. Wang, W. Zhang, Y. Qi, S. Wang, P. Liu, X. Wei, Y. Yu, W. Sun, X.-Z. Zhao and Y. Liu, *J. Alloy. Compd.*, 2021, **874**, 159916.
30. M.-S. Balogun, M. Yu, C. Li, T. Zhai, Y. Liu, X. Lu and Y. Tong, *J. Mater. Chem. A*, 2014, **2**, 10825-10829.
31. C. Yan, Y. X. Yao, X. Chen, X. B. Cheng, X. Q. Zhang, J. Q. Huang and Q. Zhang, *Angew. Chem. Int. Edit.*, 2018, **57**, 14055-14059.
32. J. Ma, L. Yu and Z. W. Fu, *Electrochim. Acta*, 2006, **51**, 4802-4814.
33. M. S. Kim, Z. Zhang, J. Wang, S. T. Oyakhire, S. C. Kim, Z. Yu, Y. Chen, D. T. Boyle, Y. Ye and Z. Huang, *ACS Nano*, 2023, **17**, 3168-3180.
34. H. Lindström, S. Södergren, A. Solbrand, H. Rensmo, J. Hjelm, A. Hagfeldt and S.-E. Lindquist, *J. Phys. Chem. B*, 1997, **101**, 7717-7722.
35. R. Liu, N. Li, E. Zhao, J. Zhao, L. Yang, W. Wang, H. Liu and C. Zeng, *Mater. Futures*, 2022, **1**, 045102.
36. K. Wang, B. Lv, Z. Wang, H. Wu, J. Xu and Q. Zhang, *Dalton Trans.*, 2020, **49**, 411-417.
37. S. Xia, X. Zhang, L. Luo, Y. Pang, J. Yang, Y. Huang and S. Zheng, *Small*, 2021, **17**, 2006002.
38. J. Du, W. Wang, M. Wan, X. Wang, G. Li, Y. Tan, C. Li, S. Tu and Y. Sun, *Adv. Energy Mater.*, 2021, **11**, 2102259.
39. W. Cao, W. Chen, M. Lu, C. Zhang, D. Tian, L. Wang and F. Yu, *J. Energy Chem.*, 2023, **76**, 648-656.
40. P. Hohenberg and W. Kohn, *Phys. Rev.*, 1964, **136**, B864.
41. P. E. Blöchl, O. Jepsen and O. K. Andersen, *Phys. Rev. B*, 1994, **49**, 16223.
42. M. C. Payne, M. P. Teter, D. C. Allan, T. Arias and a. J. Joannopoulos, *Rev. Mod. Phys.*, 1992, **64**, 1045.
43. W. Kohn and L. J. Sham, *Phys. Rev.*, 1965, **140**, A1133.
44. G. Kresse and D. Joubert, *Phys. Rev. B*, 1999, **59**, 1758.

View Article Online
DOI: 10.1039/D6TA00666C

Data for this article, including unprocessed diffraction and electrochemical data, are available from the University of Southampton institutional repository at https://doi.org/10.5258/SOTON/D3952